

Article

# Parametric Investigation of a Distributed Propulsion System on a Regional Aircraft

Donato de Rosa<sup>1,\*</sup> , Elisa Morales Tirado<sup>2</sup>  and Giuseppe Mingione<sup>1</sup><sup>1</sup> CIRA—Italian Aerospace Research Centre, Via Maiorise snc, 81043 Capua, CE, Italy; g.mingione@cira.it<sup>2</sup> Department of Industrial Engineering, University of Naples “Federico II”, 80138 Naples, NA, Italy; e.moralest6@gmail.com

\* Correspondence: d.derosa@cira.it

**Abstract:** With the mandatory requirement for more efficient aircraft due to both economic and environmental purposes, academy and industry are exploring new aircraft design opportunities including the concepts of hybrid-electric and fully electric vehicles. Within this framework, distributed electric propulsion is a key technology for future aviation, as it allows the installation of a theoretically indefinite number of small motors. The blowing effect induced by the propeller can be used to improve aerodynamic performance, hence, thanks to their reduced size, these small motors could be installed along the whole span covering the whole wing. This paper presents a study devoted to the investigation of the aerodynamic effects of distributed electric propulsion installation on a regional aircraft, computing the aerodynamic coefficients using high-fidelity CFD simulations via the RANS approach. Different propeller diameters and trust levels were analysed in climb and landing conditions, applying periodic boundary conditions on a finite span section of the wing, simulating an infinite rectangular wing. The goal of the current study is to quantify the increase of aerodynamic coefficients with reference to power off condition and report data as a function of the propeller’s characteristics. The objective is to identify and propose a simplified analytical formulation to be used in the phase of preliminary design. The implementation of such a formula in lower-fidelity tools will allow fast and reliable procedures for preliminary conceptual design.

**Keywords:** distributed propulsion; aerodynamics; computational fluid dynamics



**Citation:** de Rosa, D.; Morales Tirado, E.; Mingione, G. Parametric Investigation of a Distributed Propulsion System on a Regional Aircraft. *Aerospace* **2022**, *9*, 176. <https://doi.org/10.3390/aerospace9040176>

Academic Editor: Dimitri Mavris

Received: 2 February 2022

Accepted: 13 March 2022

Published: 23 March 2022

**Publisher’s Note:** MDPI stays neutral with regard to jurisdictional claims in published maps and institutional affiliations.



**Copyright:** © 2022 by the authors. Licensee MDPI, Basel, Switzerland. This article is an open access article distributed under the terms and conditions of the Creative Commons Attribution (CC BY) license (<https://creativecommons.org/licenses/by/4.0/>).

## 1. Introduction

Aviation has grown significantly in the last decades, and a rapid increase in total pollution attributable to air transport is evident, despite the development of more fuel-efficient turbofan or turboprop engines. The reduction of greenhouse gas emissions is a key point in Flightpath 2050 vision [1] and represents a major goal in the framework of climate preservation. To this aim, regulations on the reduction of pollutants such as CO<sub>2</sub> and NO<sub>x</sub> and noise emissions are becoming more and more rigid. In light of this new development, air transport has undertaken a redesign of existing aircraft and the proposal of innovative architectures and technologies. One of these new technologies, which is studied in this paper, is Distributed Electric Propulsion (DEP). The concept behind DEP technology is to place several small electric motors in many different locations on the aircraft, thanks to the smaller size and weight compared to conventional engines. Conceptual designs have been proposed and studied, such as the Blended Wing Body (BWB) vehicle N3-X [2,3] or the newly proposed Airbus “ZEROe” [4]. Studies on NASA’s N3-X regarding energy consumption [5], control system for propulsion [6], and noise and emissions [7] have also been published. Furthermore, ONERA started a project dedicated to DEP investigation [8], while the benefits of hybridization within the regional aircraft scale are reported in [9], as well as drag reduction achieved using DEP in [10]. A review of distributed electric concepts is also described in [11]. Two possible configurations are shown in Figure 1. The NASA SCEPTOR is depicted on the left, with propellers mounted in front of the wing leading

edge, while the ONERA AMPERE on the right side shows a cluster of ducted fans mounted on the top of the wing.

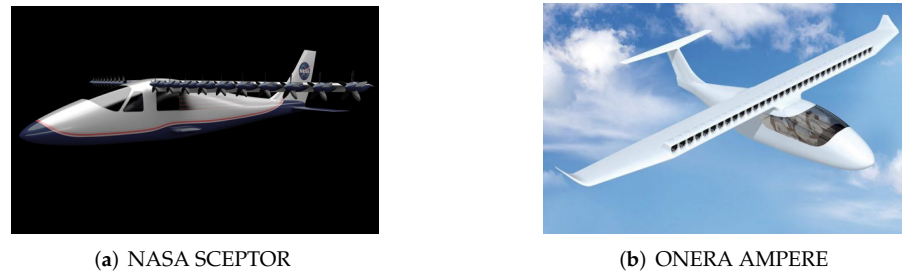


**Figure 1.** DEP Concepts.

For the SCEPTOR program, the usage of distributed electric propulsion has been investigated by Dubois et al. [12] and Deere et al. [13], while Patterson et al. [14,15] formulated an improved method for the estimation of the lift augmentation induced by DEP. The leading edge propellers are viewed as high-lift devices rather than propulsive devices as they are operated only at low-speed flight conditions to increase the speed of the airflow over the wing. The advantage is that the wing chord can be reduced, increasing the aspect ratio with consequent benefits on the efficiency of the aircraft. Contributions to DEP are not limited to aerodynamics but range from structural aspects [16] to the proper design of batteries [17], as well as involving issues in control [18].

Preliminary design methods rely on empirical formulations that have been extensively validated and verified by experimental and numerical data [19–21]. The availability of such tools allows a fast and reliable evaluation of the aerodynamic performance of an aircraft, nevertheless, most of these tools cannot be applied for configurations with distributed propulsion. The codes that allow to simulate the presence of the propeller are based on the induced increment of velocity. The scope of this work is to correlate the effect on the aerodynamic coefficients to the propeller characteristics, i.e., thrust and advance ratio, identifying the key parameters that can affect the performances of a configuration in presence of distributed propulsion and, eventually, provide a draft formulation. In order to achieve this goal, a study of the effects of DEP on lift and drag coefficients is carried out on a finite wing span section. The idea is to simulate an ideally infinite span distribution of propellers with different diameters, applying a periodic boundary condition. The aim is to identify tendency lines using the results of RANS simulations, varying the diameter of the propeller and the thrust, in order to provide a simplified formula to be used by preliminary design tools. Particularly, in Section 2 the tools used to perform the computational analysis, namely grid generator and CFD flow solver, are described. In addition, a matrix providing the complete set of test performed is given. The main results regarding the two flap configurations studied in this paper are provided in Section 3. Finally, the most important conclusions extracted from this study are pointed out in Section 4. This article represents initial research in this area, aiming at the development of design tools capable of predicting aircraft performance in presence of DEP.

## 2. Computational Analysis

In this section, the computational tools used for the grid generation and the CFD evaluation are explained. In order to reduce the effort required for the CAD and meshing, an automatic procedure to generate the geometry and the computational mesh was established. The first step is performing a linear extrusion of the airfoil, without introducing twist or sweep angles, generating a finite span wing. In the second step, the propeller, modelled as an actuator disk, is positioned in the centre of the wing span with a prescribed diameter and offset with reference to the leading edge. The final step is the grid generation using an automatic ad-hoc procedure. The presence of infinite propellers is simulated applying periodic boundary conditions at both sides of the domain. The complete test matrix studied

is also reported in this section. Moreover, it must be mentioned that two experimental campaigns are already scheduled to assess the aerodynamic and aeroacoustic effects inside CICLOP (Characterization of the Interaction between wing and Closely Operating Propeller, H2020 CS2-CFP11-2020-01 call, Grant agreement No: 101007567) and VENUS (inVestigation of distributEd propulsion Noise and its mitigation through wind tUnnel experiments and numerical Simulations, H2020 CS2-CFP10-2019-01 call, Grant agreement No 886019) European projects, respectively. Thus, these experimental data will be, then, used to validate this numerical study. In particular, the objective of CICLOP, led by Technische Universitat Braunschweig, is to close a gap in current predictions of aerodynamic effects of Distributed Electrical Propulsion and close wing coupling at high lift based on aerodynamic models and simulation, by providing high-fidelity experimental data set that will allow validation of theoretical tools and understanding of DEP aerodynamics. Additionally, VENUS, led by Università degli Studi Roma Tre, aims to understand the physics behind the aeroacoustics of DEP through deep theoretical, experimental, and numerical study. Appropriate numerical procedures for DEP noise assessment will be set up and an experimental dataset obtained in dedicated wind tunnel tests will be used both as experimental DEP noise validation reference and for providing support to the identification of the main parameters affecting DEP noise.

### 2.1. Grid Generation

To perform the CFD analysis, a parametric multiblock structured body-conformal hexahedral grid was generated using PARDOMO (parametric domain modeller) and the in-house-developed grid generator ENGRID. The domain is made of 69 blocks for three grid levels considered, and there are, approximately,  $8 \times 10^6$  cells in the finest mesh level. Particularly, 480 cells are placed on the main airfoil surface, 416 on the flap surface, 64 in the boundary layer, and 48 in the spanwise direction. The computational domain is, approximately, a squared box with 80 airfoil chords side, and the airfoil is placed in the centre.

The use of a parametric grid generation allows considerable time savings on the whole activity as, once the procedure is written, the user has to modify few parameters in the configuration file in order to obtain a new computational domain with different actuator disc size and position, as well as different flap settings. In Figure 2, the grid blocks near the airfoil, together with the airfoil surface, and the actuator disk are depicted.

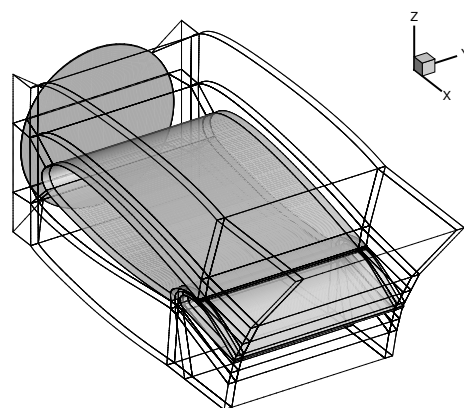


**Figure 2.** Grid blocks near the airfoil.

### 2.2. CFD Evaluation

The numerical steady-state simulations were carried out using the in-house-developed code ZEN (Zonal Euler Navier–Stokes flow solver). ZEN is a multiblock structured flow solver for steady and unsteady RANS equations, which has been developed at CIRA for more than two decades [22–24]. It is based upon cell-centred, finite-volumes formulation, with central schemes. Convergence toward steady state is achieved by explicit multistage

Runge–Kutta schemes, with acceleration techniques such as local time stepping, residual averaging, and multigrid [25]. Several turbulence models are available; all solutions in the present work were computed using the  $k - \omega$  TNT two-equation model [26].

Moreover, actuator disk boundary conditions are available, both for steady and unsteady computations [27]. The term actuator disk refers to a simplified theory that allows simulating the propeller effects by applying an appropriate impulse to the fluid crossing the surface of a disk defined by the path of a propeller blade tip. This is equivalent to applying a source term to the transport equations of the flow variables [28]. Applying the actuator disk theory, it is possible to avoid the complexity of modelling the complete rotary wing. In case of propeller aircraft, the solution of Euler or RANS equations coupled with a technique based on the actuator disk theory allows to simulate reasonably well the effect of the propeller induced field on the wing. The propeller impulse, in general cases, depends upon the time and spatial position on the disc surface. In present simulations, it is considered that impulses change only with radial distance from the propeller axis. Specifically, one actuator disk per DEP was analysed. By applying periodic boundary conditions at the wing end planes, an infinite number of corotating actuator disks is simulated. Whereas, when symmetric boundary conditions are applied at the wind end planes, alternate counter-rotating propellers are simulated. In this study, periodic boundary conditions were considered.

Finally, to monitor and determine if a CFD solution has converged, a drop of three orders of magnitude of the flow solution residuals must be reached. Additionally, considering an interval of 10,000 iterations, it was required that the standard deviation of the drag coefficient be less than 0.001. Figure 3 shows an example of convergence history for the continuity equation (left) and aerodynamic coefficients (right).

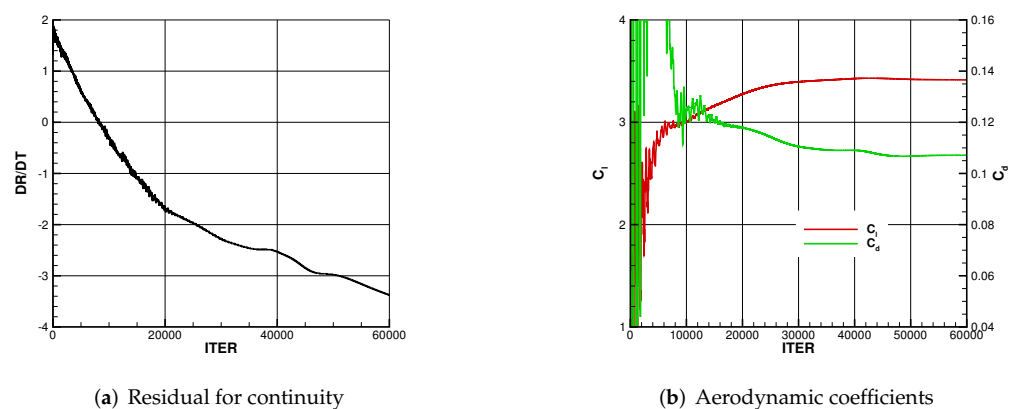


**Figure 3.** Convergence history.

### 2.3. Boundary Conditions

The main body and flap surfaces are treated as adiabatic no-slip wall, while the actuator disk boundary condition is used to simulate the propeller, as described in the previous section. On the farfield in the  $x$ - and  $z$ -directions (see Figure 2), corresponding to a squared box of side approximately equal to 80 chords, the boundary condition based on the Riemann invariants is imposed. In the  $y$ -direction, the periodic boundary condition is applied on both sides of the domain.

### 2.4. Test Matrix

The goal of this work is to perform a parametric study to evaluate the effectiveness and performance of Distributed Electric Propulsion. However, to reduce the number of analyses to perform, it was decided to start from a realistic configuration. In particular, the reference configuration considered, in terms of free-stream values and wing sectional airfoil, is based on a typical regional aircraft with 40 passengers. The aerodynamic database was built considering four DEP configurations by varying the number of propellers along the wing.

The wing span ( $b$ ) is set in order to include the propeller's diameter plus an additional 10% of the diameter, i.e., ( $b = d + 0.1d$ ). As the centre of the propeller corresponds to the centre of the domain, the previous assumption means that the distance between the tip of two adjacent propellers is equal to 10% of the diameter itself. The diameter-to-chord ratio ( $d/c$ ) is computed considering that the wing chord ( $c$ ) is 2.57 m long. A summary of the DEP configurations is provided in Table 1.

**Table 1.** Distributed Electric Propulsion Configurations.

	Test 1	Test 2	Test 3	Test 4
Number of propellers, NP	8	12	16	20
Propeller diameter [m]	2.06	1.37	1.03	0.82
Diameter–chord ratio, $d/c$	0.802	0.533	0.401	0.319

The CFD simulations were performed at standard sea level conditions  $P_\infty = 101.325$  kPa and  $\rho_\infty = 1.225$  kg/m<sup>3</sup> with a free-stream Mach number ( $M_\infty$ ) equal to 0.176 and free-stream chord-based Reynolds number ( $Re_{c_\infty}$ ) equal to  $4 \times 10^6$ . In addition, the range of angles of attack that was investigated is  $\alpha \in [-1^\circ, 18^\circ]$ . Furthermore, considering the atmospheric conditions and the Mach number, the free-stream velocity ( $V_\infty$ ) is equal to 59.84 m/s. Finally, the advance ratio ( $J = V_\infty/nD$ ), which is the ratio of the free-stream speed to the propeller tip speed, is set to 0.748815.  $n$  indicates the rotations per second of the propeller.

Two different flap deflections are considered to simulate take-off and landing conditions (see Figure 4). Moreover, different thrust ( $T$ ) levels are applied depending on the number of propellers and on the working condition (Flap A or Flap B) under study.

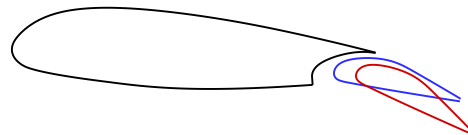


**Figure 4.** Flap deflections at Flap A (—) and Flap B (—) conditions.

A matrix for the different test cases is provided in Table 2. A total of 27 test cases were studied. Preliminary analyses (see Figure 5) showed that CTR, defined as  $CTR = T/(d^2 V^2 \rho) = C_T/J^2$  whereas  $C_T = \frac{T}{\rho n^2 D^4}$ , the Renard thrust coefficient, is a crucial parameter. As a consequence, it was decided to consider CTR as a variable for carrying out the parametric study. The second variable considered is the diameter-to-chord ratio  $d/c$ , as its effect on lift augmentation is already presented in [15].

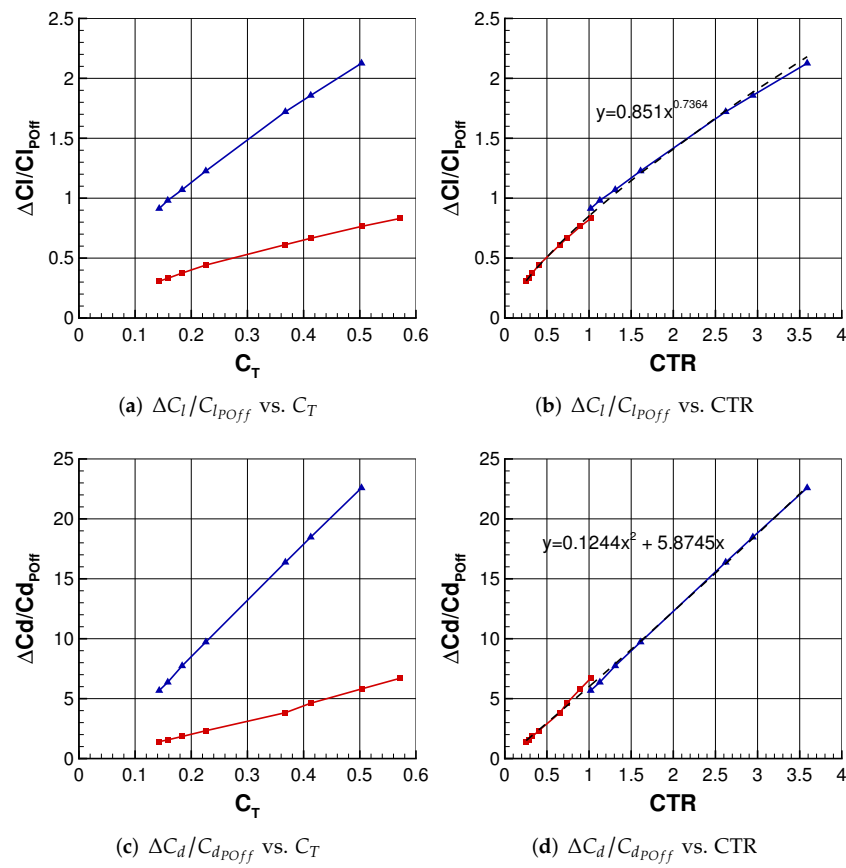


**Figure 5.** Increment of lift and drag coefficients for the test at  $V_{\infty} = 59.84$  m/s (—■—) and  $V_{\infty} = 29.92$  m/s (—▲—). The corresponding tendency lines are in dashed (---).

**Table 2.** Test cases matrix.

	$d/c$	$T$ [N]	CTR	Flap A	Flap B
Case A1	0.802	4745	0.2549	✓	✓
Case B1		5250	0.2820	✓	✗
Case C1		6100	0.3277	✓	✗
Case D1		7500	0.4029	✓	✓
Case E1		12,200	0.6554	✓	✓
Case F1		13,700	0.7360	✓	✗
Case G1		16,700	0.8971	✓	✓
Case A2	0.533	3500	0.4251	✓	✗
Case B2		5000	0.6073	✓	✗
Case C2		5400	0.6559	✓	✗
Case D2		7420	0.9012	✓	✗
Case E2		8050	0.9778	✓	✗
Case A3	0.401	2625	0.5641	✓	✗
Case B3		3050	0.6554	✓	✗
Case C3		3750	0.8058	✓	✗
Case D3		4200	0.9025	✓	✗
Case E3		4550	0.9777	✓	✗
Case A4	0.319	2100	0.7120	✓	✗
Case B4		2400	0.8137	✓	✗
Case C4		3000	1.0171	✓	✗
Case D4		3140	1.0646	✓	✗
Case E4		3380	1.1460	✓	✗

### 3. Results

In this section, the main results obtained by CFD evaluations are presented divided in Flap A and Flap B configurations. The polar curves of the test cases with the highest  $d/c$  ratio are provided for both configurations. In addition, for each set of test ( $d/c = 0.802, 0.533, 0.401, 0.319$ ), the increment in percentage of the aerodynamic coefficients is reported for three angles of attack [ $8^\circ, 10^\circ$  and  $12^\circ$ ]. The increment is calculated with respect to the corresponding power-off condition. The increments are given with reference to the previously defined thrust coefficient (CTR).

The motivation behind the definition of this parameter is shown in Figure 5. In particular, the parameter CTR is introduced to identify a tendency line for the increment of the aerodynamic coefficients, even if different values of  $J$  are used. Let us vary the advance ratio by halving the free-stream velocity, and keeping constant the number of propellers and the rotations per second. Thus, the working conditions of the propeller are changed, but the propeller characteristics are maintained. The reference case is the take-off condition with  $d/c = 0.802$  and  $n$  equal to 38.79 rps at nominal free-stream velocity ( $V_\infty = 59.84$  m/s). The thrust levels analysed are those in Table 2. The angle of attack is  $\alpha = 8^\circ$  and the simulations are performed at standard sea level conditions. The same conditions are analysed with a different free-stream velocity ( $V_\infty = 29.92$  m/s). An additional thrust level ( $T = 19,000$  N) was also analysed for the case with free-stream velocity equal to 59.84 m/s. This thrust level was analysed in order to have a CTR point in common (CTR  $\approx 1.0$ ) for the test cases at both velocities.

The current set of input values returns the same  $C_T$  for both conditions, but different  $J$  and, as a consequence, different CTR. Figure 5 clearly shows the reason behind the choice of representing the increment of aerodynamic coefficients vs. CTR. In fact, the results tend to lay on a continuous curve. In this way, tendency lines are built based on the obtained results for lift and drag coefficients. For the lift coefficient, the authors propose a power trend, considering that the lift can increase with thrust up to a limit that is given by the performance of the airfoil and for CTR = 0, the condition of zero increment in lift is automatically satisfied. Differently, for the drag coefficient, a polynomial function of second order and zero intercept is selected since an increase in drag is always expected when the thrust rises, and at zero thrust, power-off conditions are found. It must be remarked that these tendency lines were selected taking into account only numerical data, hence, they have to be considered as a starting point to be improved with additional data and assessed when experiments become available.

#### 3.1. Flap A Working Conditions

Firstly, the polar curves obtained for the configuration with  $d/c = 0.802$  are provided in Figure 6. In particular, the polar curves for the test cases A1-G1 (see Table 2) are compared with the power-off conditions. Note that, data at angles of attack after stall conditions are not provided. In addition, only steady simulations were completed. Therefore, if at some angle of attack  $C_l$  and  $C_d$  are not given, this is due to the unsteady behaviour found in the CFD evaluation. A more in-depth analysis was carried out for some cases where unsteadiness was observed. At angles of attack prior to the stall condition, a time-accurate convergence led to a steady-state solution. In the post-stall region, periodic and nonperiodic solutions were achieved. As an exhaustive analysis on the performance of the wing-propeller setup was beyond the scope of the current research, these cases were bypassed.

As expected, there is an increase in lift and drag coefficients at any power-on condition with respect to power-off, being at maximum at the highest thrust studied. Moreover, the lift polar curves of power-on conditions present a slope ( $C_{l_\alpha}$ ) higher than the power-off condition.

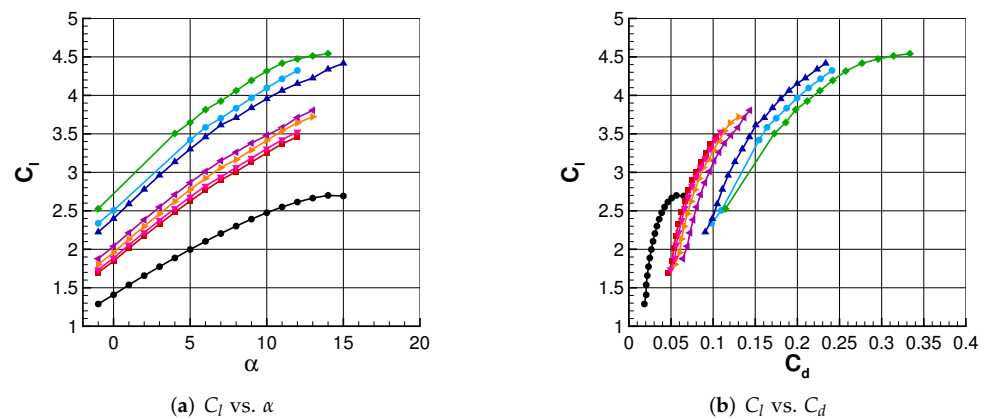


**Figure 6.** Polar curves comparison of the test cases  $d/c = 0.802$  with respect to power-off condition (—●—). Test case A1 (—■—), B1 (—▼—), C1 (—►—), D1 (—◄—), E1 (—▲—), F1 (—●—), and G1 (—◆—).

Furthermore, the increment (in percentage) of the aerodynamic coefficients is reported at three different angles of attack ( $\alpha = 8^\circ, 10^\circ$ , and  $12^\circ$ ) in Figures 7–9.

Regarding the lift coefficient (plots on the left in Figures 7–9), it is observed that the increment provided by the power-on conditions decreases with a decreasing  $d/c$  ratio. This result is in agreement with the one presented by Gallani et al. [29]. Hence, the configuration with  $d/c = 0.802$  is the most promising configuration. In addition, the choice of a power trend to represent the increment on lift is suitable for the two higher diameter–chord ratios ( $d/c = 0.802$  and  $0.533$ ) at all studied angles of attack. However, when the ratio further decreases ( $d/c = 0.401$  and  $0.319$ ), some discrepancies appear for  $\alpha = 10^\circ$  and  $12^\circ$ .

Considering, now, the drag coefficient (plots on the right in Figures 7–9), a decrease in  $\Delta C_d/C_{d_{poff}}$  is observed when  $d/c$  decreases. Nevertheless, this decrease on the aerodynamic coefficient is not as obvious as in the case of the  $C_l$ . Particularly, at  $\alpha = 8^\circ$ , similar increments of the drag coefficient are obtained for configurations  $d/c = 0.802$  and  $0.533$ . This behaviour is also found between configurations  $d/c = 0.401$  and  $0.319$  at an angle of attack equal to  $12^\circ$ . Moreover, it must be mentioned that a proper fitting of the increment of drag coefficient by using a quadratic polynomial is confirmed. Only at  $\alpha = 10^\circ$  for  $d/c = 0.319$  some discrepancies appeared.

From the previous considerations, it can be concluded that the configuration with the highest  $d/c$  ratio provides the best performance, greatest aerodynamic efficiency, at all angles of attack. In contrast, the configuration with the lowest  $d/c$  ratio is the worst, not only regarding performance, but also in terms of fitting. The selected curves, generally, do not fit properly the studied data.

Moreover, also interesting is the effect of the angle of attack on the increment of the aerodynamic coefficients at a fixed configuration. Specifically, this was studied at the most promising configuration ( $d/c = 0.802$ ), and it is shown in Figure 10.

In terms of lift and drag coefficients, the angle of attack has barely any effect on the provided increment by the power-on conditions, as shown in Figure 10. For both aerodynamic coefficients, the maximum difference between increments at different angles of attack is found at the highest values of CTR, giving the highest increment the smallest angle of attack ( $\alpha = 8^\circ$ ).

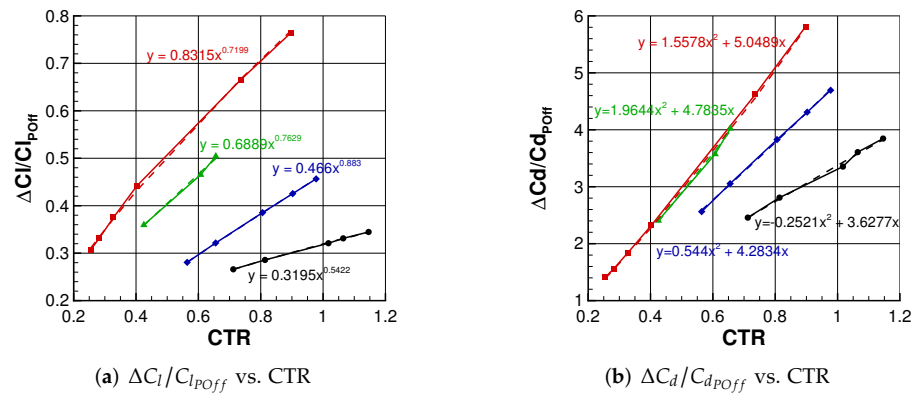


**Figure 7.** Increment of lift (left) and drag (right) coefficients at  $\alpha = 8^\circ$  for  $d/c = 0.802$  (—■—),  $d/c = 0.533$  (—▲—),  $d/c = 0.401$  (—◆—), and  $d/c = 0.319$  (—●—). In addition, their corresponding tendency lines are dashed.

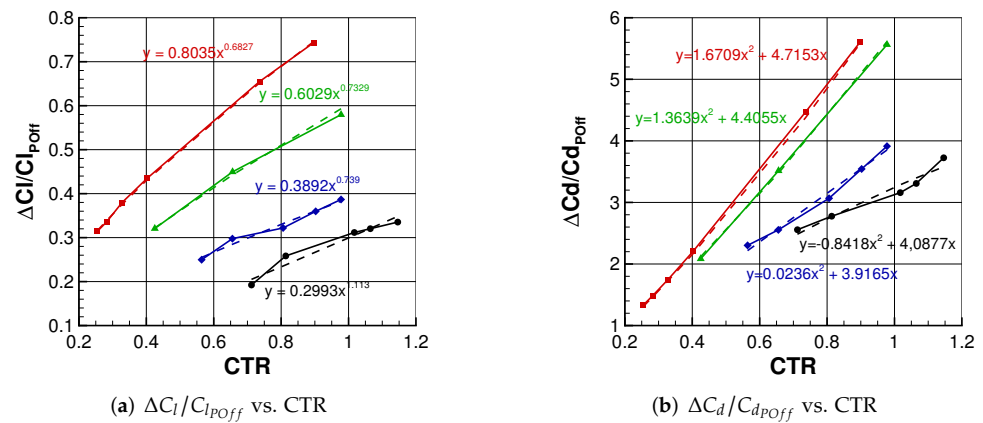


**Figure 8.** Increment of lift (left) and drag (right) coefficients at  $\alpha = 10^\circ$  for  $d/c = 0.802$  (—■—),  $d/c = 0.533$  (—▲—),  $d/c = 0.401$  (—◆—), and  $d/c = 0.319$  (—●—). In addition, their corresponding tendency lines are dashed.

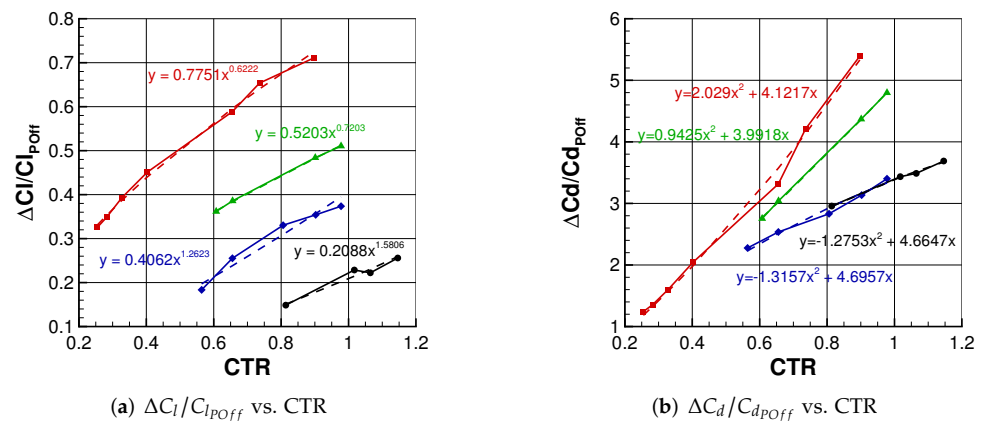


**Figure 9.** Increment of lift (left) and drag (right) coefficients at  $\alpha = 12^\circ$  for  $d/c = 0.802$  (—■—),  $d/c = 0.533$  (—▲—),  $d/c = 0.401$  (—◆—), and  $d/c = 0.319$  (—●—). In addition, their corresponding tendency lines are dashed.

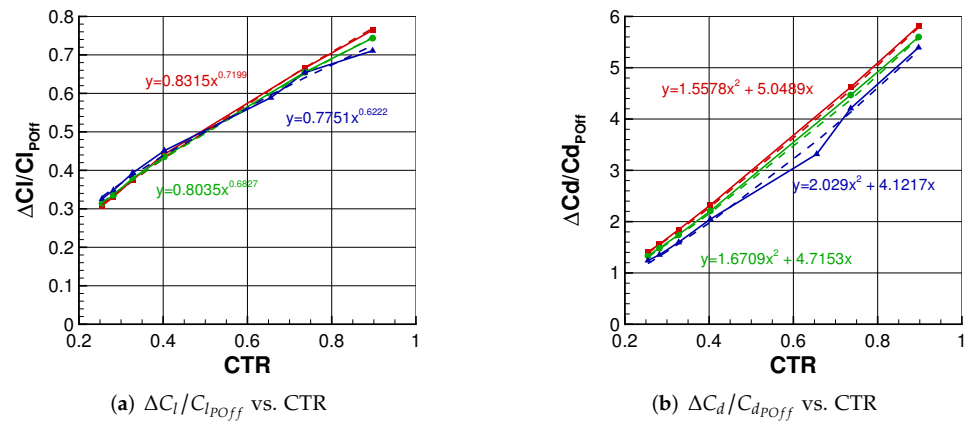


**Figure 10.** Increment of lift and drag coefficients at  $\alpha = 8^\circ$  (—■—),  $\alpha = 10^\circ$  (—●—), and  $\alpha = 12^\circ$  (—▲—) for  $d/c = 0.802$ . In addition, their corresponding tendency lines are dashed.

On the base of the actual results, for the Flap A condition, the following formula are proposed:

$$\frac{\Delta C_l}{C_{lPOff}} = c_1 \ln\left(\frac{d}{c} + c_2\right) CTR^{c_3} \frac{d}{c}^{c_4} \quad (1)$$

$$\frac{\Delta C_d}{C_{dPOff}} = \max\left[ c_5 + c_6 \frac{d}{c} + c_7 CTR + c_8 \left(\frac{d}{c}\right)^2 + c_9 \frac{d}{c} CTR + c_{10} CTR^2; 0 \right] \quad (2)$$

The constants in Equations (1) and (2) are reported in Table 3.

**Table 3.** Constants.

$c_1$	$c_2$	$c_3$	$c_4$	$c_5$	$c_6$	$c_7$	$c_8$	$c_9$	$c_{10}$
1.563	0.8813	0.2026	0.5203	−0.473	6.53	−1.135	−7.744	8.4	0.9283

The formula is tuned to better approximate the solutions at high  $d/c$ , losing accuracy towards low values of the diameter–chord ratio. It was preferred to match the results obtained at the highest values of  $d/c$  ratio as they provide the best increments of performance. A 3 – D plot of the formula in Equations (1) and (2) is shown in Figure 11.

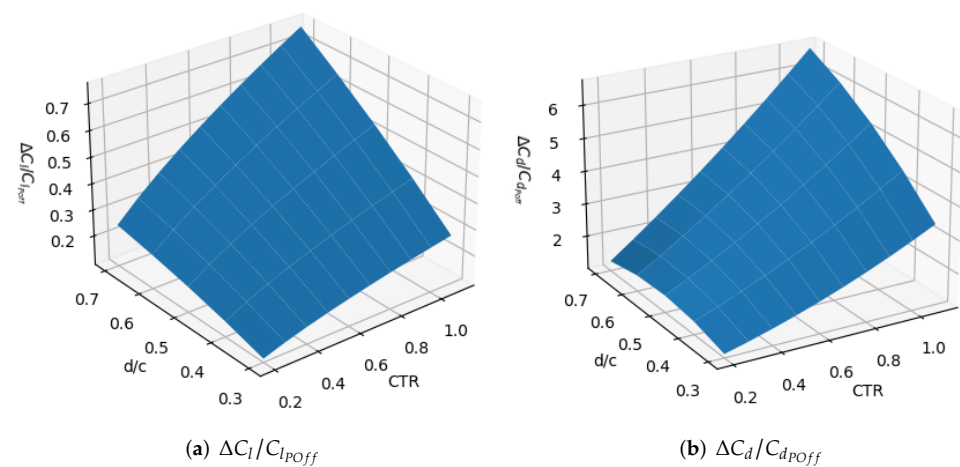


**Figure 11.** Surface plot of estimated increment of aerodynamic coefficients.

### 3.2. Flap B Working Conditions

For the second flap condition, only the configuration  $d/c = 0.802$  is considered. This decision was made after studying Flap A conditions, since the increment of the aerodynamic coefficients of configurations with lower  $d/c$  ratios are less than those obtained for  $d/c = 0.802$ . In addition, some of the thrust was also discarded considering that the objective is to verify if the proposed trends at Flap A conditions are also anticipated for Flap B conditions.

In Figure 12, a comparison of the polar curves between power-on and power-off conditions is shown. As it was observed for the Flap A condition, both lift and drag coefficients increase at power-on conditions. Contrary to what was observed for the Flap A condition, an increase in  $C_{l\alpha}$  is not anticipated. Furthermore, the lift curves for the two highest thrust conditions are in a near-stall region. This behaviour is correlated to the different settings both for the larger flap deflection and to the increased gap and overlap distance.

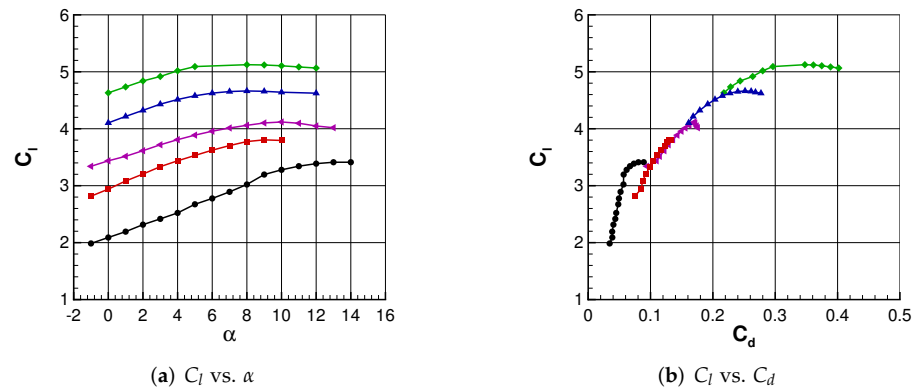


**Figure 12.** Polar curves comparison of the test cases with NP = 8 with respect to power-off condition (—●—). Test case A1 (—■—), D1 (—▲—), E1 (—▲—), and G1 (—◆—).

Furthermore, in Figure 13, the increment on the aerodynamic coefficients provided by the power-on conditions is going to be compared at three different angles of attack ( $\alpha = 8^\circ, 10^\circ$  and  $12^\circ$ ). Differing from what was estimated for Flap A conditions, the angle of attack has a visible effect on the lift coefficient increment, as a direct consequence of comparing a near-stall condition for the power-on configurations. In particular, the highest increase of  $\Delta C_l / C_{l_{POff}}$  is obtained at  $\alpha = 8^\circ$ . Regarding the drag coefficient, no remarkable effect is observed between  $8^\circ$  and  $10^\circ$ . Nevertheless, at  $\alpha = 12^\circ$  a reduction with respect to the other two angles-of-attack is noticed.

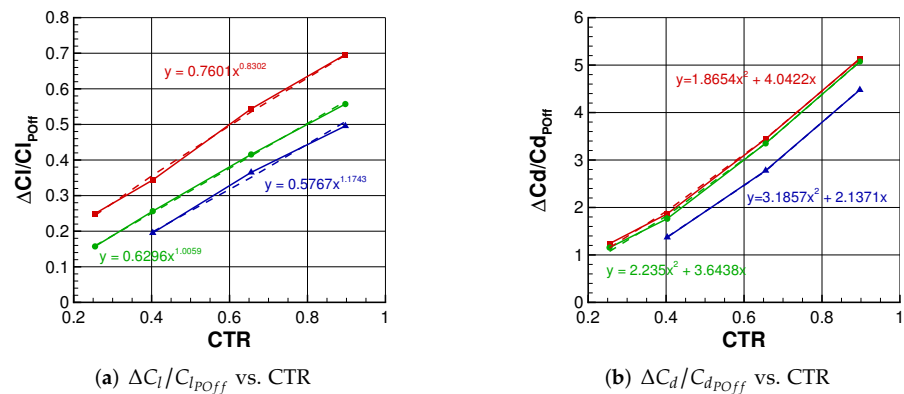


**Figure 13.** Increment of lift and drag coefficients at  $\alpha = 8^\circ$  (—■—),  $\alpha = 10^\circ$  (—●—), and  $\alpha = 12^\circ$  (—▲—). In addition, their corresponding tendency lines are dashed.

#### 4. Conclusions

This study aimed to identify and propose a simplified analytical formulation to be used during the preliminary design phase that characterises the aerodynamic performances of a wing in the presence of Distributed Electric Propulsion (DEP). Firstly, the parameters that most influence the maximum lift coefficient were identified. In order to allow a generalisation, these parameters were collected in a nondimensional representation, i.e.,  $d/c$  and CTR. Then, the parametric study was carried out to find the semi-empirical formulae that characterise the effects of using DEP. Four different sets of propellers were chosen and, for each set, several thrust levels were selected. A finite wing span section with one propeller, simulated as an actuator disk, was analysed using periodic boundary conditions. With this hypothesis, an infinite wing with an infinite number of propellers was simulated.

For each  $d/c$  ratio, aerodynamic coefficients were reported as increment with reference to the corresponding power-off condition. The results showed that performance in terms of lift coefficient improves with increasing  $d/c$  ratio. A modified formulation of the Renard thrust coefficient was introduced. The increments of lift and drag coefficients plotted as function of this coefficient tend to overlap with each other at fixed  $d/c$ . With this representation, it is possible to build a fitting function.

Three angles of attack for the Flap A condition, namely,  $\alpha = 8^\circ, 10^\circ, 12^\circ$ , were selected as reference and reported results showed that, for the lift coefficient, a power trend fitting curve approximates well the numerical data. A similar conclusion is achieved for drag coefficients, where a second-order polynomial function and zero intercept are proposed. A fitting surface as a function of  $d/c$  and CTR is also proposed based on available data.

Flap B configuration was considered only for the highest  $d/c$  ratio. A comprehensive analysis of the results to be compared with Flap A configuration was not possible for the selected angles. In fact, for power-on condition, the data refer to the stall region of lift curve. Nevertheless, Flap B configuration presents a similar trend for the increase of the aerodynamic coefficients with reference to Flap A.

Experimental data are needed to assess this preliminary numerical activity and two experimental test campaigns are currently scheduled. Wind tunnel test campaigns will be carried out in the framework of European funded programme and, in particular, in the CICLOP project for the aerodynamic characterisation and VENUS project for the aeroacoustic one.

**Author Contributions:** Conceptualization, G.M.; Data curation, E.M.T.; Formal analysis, D.d.R. and E.M.T.; Software, D.d.R.; Visualization, D.d.R. and E.M.T.; Writing—original draft, D.d.R. and E.M.T.; Writing—review & editing, D.d.R. and E.M.T. All authors have read and agreed to the published version of the manuscript.

**Funding:** This research was funded by the Italian Ministry of University and Research in the PROSIB project, PON grant number PROSIB ARS01\_00297.

**Institutional Review Board Statement:** Not applicable.

**Informed Consent Statement:** Not applicable.

**Data Availability Statement:** The data presented in this study are available on request from the corresponding author.

**Conflicts of Interest:** The authors declare no conflict of interest.

#### References

1. Darecki, M.; Edelstenne, C.; Enders, T.; Fernandez, E.; Hartman, P.; Herteman, J.P.; Kerkloh, M.; King, I.; Ky, P.; Mathieu, M.; et al. Flightpath 2050. 2011. p. 28. Available online: <https://op.europa.eu/en/publication-detail/-/publication/7d834950-1f5e-480f-ab70-ab96e4a0a0ad/language-en> (accessed on 1 February 2022). [CrossRef]
2. Kim, H.D.; Brown, G.V.; Felder, J.L. Distributed Turboelectric Propulsion for Hybrid Wing Body Aircraft. In Proceedings of the 2008 International Powered Lift Conference Royal Aeronautical Society, London, UK, 20–24 July 2008.

3. Armstrong, M.J.; Ross, C.A.H.; Blackwelder, M.J.; Rajashekara, K. Trade Studies for NASA N3-X Turboelectric Distributed Propulsion System Electrical Power System Architecture. *SAE Int. J. Aerosp.* **2012**, *5*, 325. [[CrossRef](#)]
4. Airbus. Airbus Reveals New Zero-Emission Concept Aircraft. 2020. Available online: <https://www.airbus.com/en/newsroom/press-releases/2020-09-airbus-reveals-new-zero-emission-concept-aircraft> (accessed on 1 February 2022).
5. Felder, J.; Tong, M.; Chu, J. Sensitivity of Mission Energy Consumption to Turboelectric Distributed Propulsion Design Assumptions on the N3-X Hybrid Wing Body Aircraft. In Proceedings of the 48th AIAA/ASME/SAE/ASEE Joint Propulsion Conference & Exhibit, Atlanta, GA, USA, 30 July–1 August 2012; American Institute of Aeronautics and Astronautics: Reston, VA, USA, 2012. [[CrossRef](#)]
6. Choi, B.; Brown, G.V.; Morrison, C.; Dever, T. Propulsion Electric Grid Simulator (PEGS) for Future Turboelectric Distributed Propulsion Aircraft. In Proceedings of the 12th International Energy Conversion Engineering Conference, Cleveland, OH, USA, 28–30 July 2014; American Institute of Aeronautics and Astronautics: Reston, VA, USA, 2014. [[CrossRef](#)]
7. Berton, J.J.; Haller, W.J. A Noise and Emissions Assessment of the N3-X Transport. In Proceedings of the 52nd Aerospace Sciences Meeting, Prince George’s County, MD, USA, 13–17 January 2014; American Institute of Aeronautics and Astronautics: Reston, VA, USA, 2014. [[CrossRef](#)]
8. Hermetz, J.; Ridel, M.; Doll, C. Distributed electric propulsion for small business aircraft a concept-plane for key-technologies investigations. In Proceedings of the Twelfth International Conference on Autonomic and Autonomous Systems, ICAS 2016, Lisbon, Portugal, 26–30 June 2016; p. 10.
9. Thauvin, J.; Barraud, G.; Budinger, M.; Roboam, X.; Leray, D.; Sareni, B. Hybrid Regional Aircraft: A Comparative Review of New Potentials Enabled by Electric Power. In Proceedings of the 52nd AIAA/SAE/ASEE Joint Propulsion Conference, Salt Lake City, UT, USA, 25–27 July 2016; American Institute of Aeronautics and Astronautics: Reston, VA, USA, 2016. [[CrossRef](#)]
10. Stoll, A.M.; Bevirt, J.B.; Moore, M.D.; Fredericks, W.J.; Borer, N.K. Drag reduction through distributed electric propulsion. In Proceedings of the AIAA AVIATION 2014—14th AIAA Aviation Technology, Integration, and Operations Conference, Atlanta, GA, USA, 16–20 June 2014; American Institute of Aeronautics and Astronautics: Reston, VA, USA, 2014. [[CrossRef](#)]
11. Kim, H.D.; Perry, A.T.; Ansell, P.J. A Review of Distributed Electric Propulsion Concepts for Air Vehicle Technology. In Proceedings of the 2018 AIAA/IEEE Electric Aircraft Technologies Symposium, EATS 2018, Cincinnati, OH, USA, 12–14 July 2018; American Institute of Aeronautics and Astronautics: Reston, VA, USA, 2018. [[CrossRef](#)]
12. Dubois, A.; van der Geest, M.; Bevirt, J.; Christie, R.; Borer, N.K.; Clarke, S.C. Design of an Electric Propulsion System for SCEPTOR’s Outboard Nacelle. In Proceedings of the 16th AIAA Aviation Technology, Integration, and Operations Conference, Washington, DC, USA, 13–17 June 2016; American Institute of Aeronautics and Astronautics: Reston, VA, USA, 2016. [[CrossRef](#)]
13. Deere, K.A.; Viken, J.K.; Viken, S.; Carter, M.B.; Wiese, M.; Farr, N. Computational Analysis of a Wing Designed for the X-57 Distributed Electric Propulsion Aircraft. In Proceedings of the 35th AIAA Applied Aerodynamics Conference, Denver, CO, USA, 5–9 June 2017; American Institute of Aeronautics and Astronautics: Reston, VA, USA, 2017. [[CrossRef](#)]
14. Patterson, M.D.; Daskilewicz, M.J.; German, B. Simplified Aerodynamics Models to Predict the Effects of Upstream Propellers on Wing Lift. In Proceedings of the 53rd AIAA Aerospace Sciences Meeting, Kissimmee, FL, USA, 5–9 January 2015; American Institute of Aeronautics and Astronautics: Reston, VA, USA, 2015. [[CrossRef](#)]
15. Patterson, M.D.; Derlaga, J.M.; Borer, N.K. High-Lift Propeller System Configuration Selection for NASA’s SCEPTOR Distributed Electric Propulsion Flight Demonstrator. In Proceedings of the 16th AIAA Aviation Technology, Integration, and Operations Conference, Washington, DC, USA, 13–17 June 2016; American Institute of Aeronautics and Astronautics: Reston, VA, USA, 2016. [[CrossRef](#)]
16. Čerňan, J.; Janovec, M.; Škultéty, F. The stress analysis of air turbine driven propeller blade. *Transp. Res. Procedia* **2020**, *51*, 293–303. [[CrossRef](#)]
17. Janovec, M.; Čerňan, J.; Škultéty, F.; Novák, A. Design of Batteries for a Hybrid Propulsion System of a Training Aircraft. *Energies* **2021**, *15*, 49. [[CrossRef](#)]
18. Burston, M.; Ranasinghe, K.; Gardi, A.; Parezanović, V.; Ajaj, R.; Sabatini, R. Design principles and digital control of advanced distributed propulsion systems. *Energy* **2022**, *241*, 122788. [[CrossRef](#)]
19. Raymer, D. *Aircraft Design: A Conceptual Approach, Sixth Edition*; American Institute of Aeronautics and Astronautics, Inc.: Washington, DC, USA, 2018. [[CrossRef](#)]
20. Springer, A.M. (Ed.) *Aerospace Design: Aircraft, Spacecraft, and the Art of Modern Flight*; Merrell Publisher: London, UK, 2004; Volume 41, pp. 41–4620.
21. Roskam, J. *Airplane Design: Preliminary Sizing of Airplanes*; Design, Analysis and Research Corporation: Lawrence, KS, USA, 2015.
22. Catalano, P.; Amato, M. An evaluation of {RANS} turbulence modelling for aerodynamic applications. *Aerosp. Sci. Technol.* **2003**, *7*, 493–509. [[CrossRef](#)]
23. Marongiu, C.; Catalano, P.; Amato, M.; Iaccarino, G. U-{ZEN}: A Computational Tool Solving U-Rans Equations for Industrial Unsteady Applications. In Proceedings of the 34th AIAA Fluid Dynamics Conference and Exhibit, Portland, OR, USA, 28 June–1 July 2004; American Institute of Aeronautics and Astronautics: Reston, VA, USA, 2004. [[CrossRef](#)]
24. Marongiu, C.; Panizza, A.; Vitagliano, P.L. A moving grid method for unsteady flow computations. In Proceedings of the 18th AIAA Computational Fluid Dynamics Conference, Miami, FL, USA, 25–28 June 2007; p. 4470.
25. Jameson, A. Time dependent calculations using multigrid, with applications to unsteady flows past airfoils and wings. In Proceedings of the 10th Computational Fluid Dynamics Conference, Honolulu, HI, USA, 24–26 June 1991; p. 1596.
26. Kok, J.C. Resolving the dependence on freestream values for the k-turbulence model. *AIAA J.* **2000**, *38*, 1292–1295. [[CrossRef](#)]

27. Vitagliano, P.L. Deliverable D3.3.2-5c: “An Actuator Disk Model for Unsteady Flow Simulations”, CESAR Integrated project AIP5-CT-2006-030888. Technical Report CIRA-CF-10-0023, CIRA. 2010. Available online: [https://trimis.ec.europa.eu/sites/default/files/project/documents/20120716\\_094200\\_52135\\_CESAR\\_Publishable\\_Activity\\_Report.pdf](https://trimis.ec.europa.eu/sites/default/files/project/documents/20120716_094200_52135_CESAR_Publishable_Activity_Report.pdf) (accessed on 1 February 2022).
28. Le Chuiton, F. Actuator disc modelling for helicopter rotors. *Aerosp. Sci. Technol.* **2004**, *8*, 285–297. [[CrossRef](#)]
29. Gallani, M.A.; Góes, L.C.; Nerosky, L.A. Effects of distributed electric propulsion on the performance of a general aviation aircraft. In Proceedings of the AIAA Propulsion and Energy 2020 Forum, New Orleans, LA, USA, 24–28 August 2020; American Institute of Aeronautics and Astronautics: Reston, VA, USA, 2020; pp. 1–16. [[CrossRef](#)]